Interactions of Estuarine Shoreline Infrastructure With Multiscale Sea Level Variability

Wang, Ruo-Qian; Herdman, Liv M.; Erikson, Li; Barnard, Patrick; Hummel, Michelle; Stacey, Mark T.

Published in:
Journal of Geophysical Research: Oceans

DOI:
10.1002/2017JC012730

Publication date:
2017

Document Version
Publisher's PDF, also known as Version of record

AGU PUBLICATIONS

JGR

Journal of Geophysical Research: Oceans

RESEARCH ARTICLE

10.1002/2017JC012730

Interactions of Estuarine Shoreline Infrastructure With Multiscale Sea Level Variability

Ruo-Qian Wang[1], Liv M. Herdman[2], Li Erikson[2], Patrick Barnard[2], Michelle Hummel[1], and Mark T. Stacey[1]

[1]Department of Civil and Environmental Engineering, University of California, Berkeley, Berkeley, CA, USA, [2]Pacific Coastal and Marine Science Center, United States Geological Survey, Santa Cruz, CA, USA

Key Points:
- The diffusion of multiday water level events is studied with tidal motions and the interaction with shoreline accommodation schemes
- Multiday high water events do not significantly alter the tidal dynamics, but the tides are important to the evolution of multiday events
- The effect of coastal protection can be estimated by calculating the equivalent local diffusion coefficient with inverse modeling

Correspondence to:
M. T. Stacey,
mstacey@berkeley.edu

Citation:
Wang, R.-Q., Herdman, L. M., Erikson, L., Barnard, P., Hummel, M., & Stacey, M. T. (2017). Interactions of estuarine shoreline infrastructure with multiscale sea level variability. *Journal of Geophysical Research: Oceans*, *122*, 9962–9979. https://doi.org/10.1002/2017JC012730

Received 24 JAN 2017
Accepted 4 SEP 2017
Accepted article online 26 SEP 2017
Published online 15 DEC 2017

Abstract Sea level rise increases the risk of storms and other short-term water-rise events, because it sets a higher water level such that coastal surges become more likely to overtop protections and cause floods. To protect coastal communities, it is necessary to understand the interaction among multiday and tidal sea level variabilities, coastal infrastructure, and sea level rise. We performed a series of numerical simulations for San Francisco Bay to examine two shoreline scenarios and a series of short-term and long-term sea level variations. The two shoreline configurations include the existing topography and a coherent full-bay containment that follows the existing land boundary with an impermeable wall. The sea level variability consists of a half-meter perturbation, with duration ranging from 2 days to permanent (i.e., sea level rise). The extent of coastal flooding was found to increase with the duration of the high-water-level event. The nonlinear interaction between these intermediate scale events and astronomical tidal forcing only contributes ~1% of the tidal heights; at the same time, the tides are found to be a dominant factor in establishing the evolution and diffusion of multiday high water events. Establishing containment at existing shorelines can change the tidal height spectrum up to 5%, and the impact of this shoreline structure appears stronger in the low-frequency range. To interpret the spatial and temporal variability at a wide range of frequencies, Optimal Dynamic Mode Decomposition is introduced to analyze the coastal processes and an inverse method is applied to determine the coefficients of a 1-D diffusion wave model that quantify the impact of bottom roughness, tidal basin geometry, and shoreline configuration on the high water events.

1. Introduction

Oceanic water levels vary on a wide range of time scales, with forcing from astronomical tides, synoptic weather events, annual and interannual climatic variability, and long-term climate change. From the perspective of coastal flooding, these various forcing mechanisms together define high-water-level (HWL) events that define flooding patterns around the perimeter of coastal embayments, which are frequently urbanized and developed. Recent work has examined how tidal forcing and flooding may be influenced by long-term change in mean sea levels (Holleman & Stacey, 2014), but the wide range of other time scales active in the world's oceans, particularly those of days or weeks, has received limited attention. While interaction between these frequencies is to be expected, several questions emerge when examining these intermediate time scale events; an important question that relates to planning and management of the threat of sea level rise is whether we can interpret a HWL event as a preview of long-term sea level rise (SLR). If so, how long should the HWL event be? And to what extent can the HWL event mimic SLR? To answer these questions, we need to examine the impact of the duration of HWL events on the tidal dynamics.

The driving mechanisms of the tidal dynamics span a wide range of time scales, including the long-term scale of SLR, the monthly scale of freshwater discharges, the daily scale of HWL events, and the hourly scale of astronomical tidal oscillations. Nonlinear effects produce overtides, and the interaction of different tidal constituents produces compound tides, such as M_{sf}. In the past, the overtides and compound tides have been studied in the context of tidal asymmetry, which has been reviewed by Pugh (2004), Woodworth et al. (2005), and Castanedo et al. (2007). The early studies focused on one-dimensional analytical models to explain the generation of overtides and compound tides (Friedrichs & Aubrey, 1988, 1994; Parker, 1984, 1991; Pugh, 1987). Numerical simulation was later introduced to test the developed theoretical models and explain field observations (Le Provost, 1991; Walters & Werner, 1991; Wang et al., 1999). The recent studies

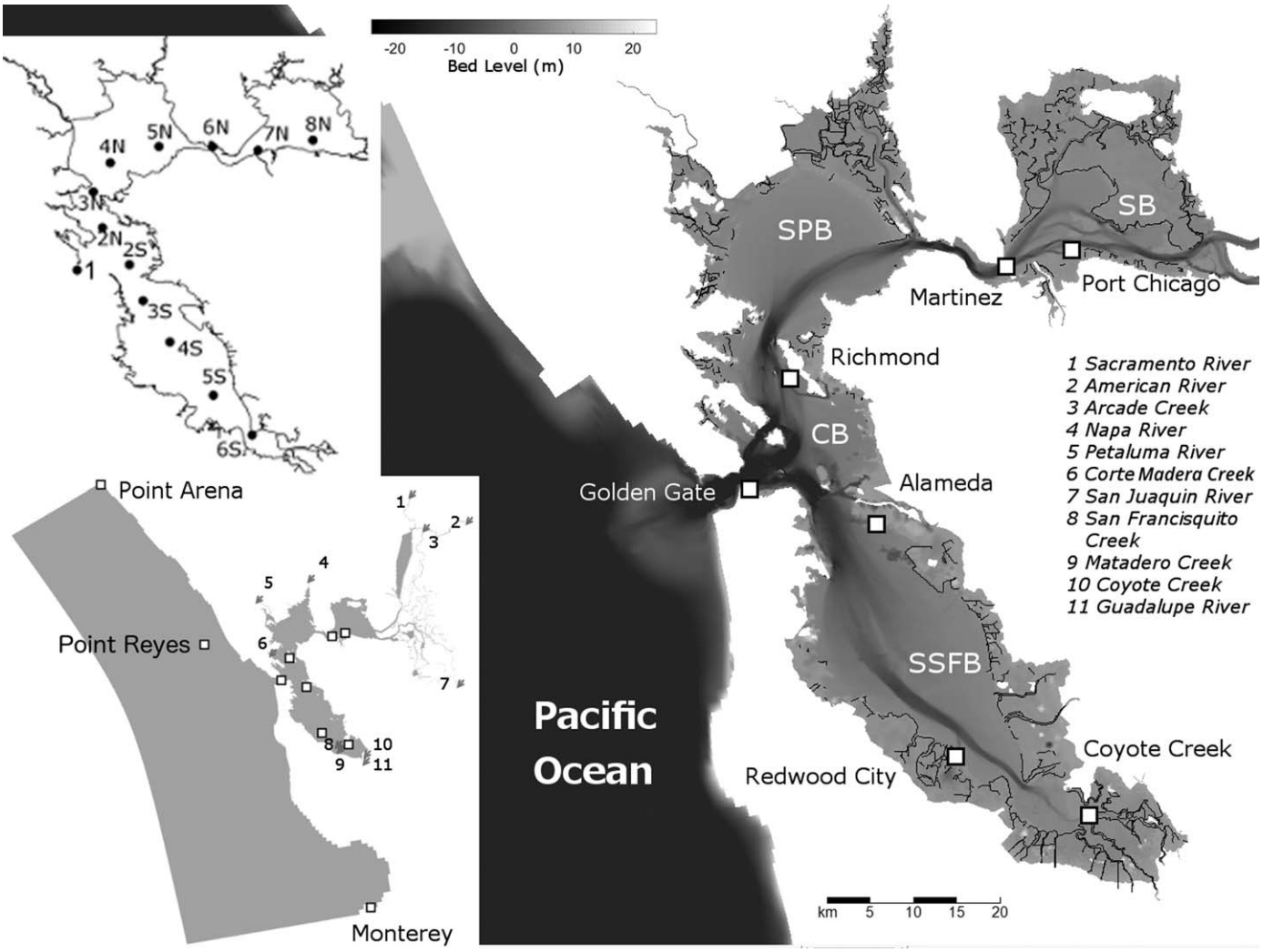

Figure 1. The computational domain covers SF Bay and an open ocean area. The color represents the depth of the bathymetry from −24 to 24 m. The gray dash line represents the position of the seawalls. The squares denote the position of the observation sites. The labeled number indicates the source location of the freshwater discharge, which is named on the right side of the figure. The names of the tidal basins in San Francisco (SF) Bay are South SF Bay (SSFB), Central Bay (CB), San Pablo Bay (SPB), and Suisun Bay (SB). The map extends 37.40°N–38.29°N and 121.76°W–123.22°W.

focused on the interaction of freshwater discharge and tidal constituents, e.g., Sassi and Hoitink (2013) and Jay et al. (2015), but less attention has been paid on the interaction between the daily scale HWL events and the astronomical tidal constituents.

The tidal dynamics are subject to the impact of SLR, which has received increased research interest recently. For example, Pickering et al. (2012), Pelling and Green (2014), and Idier et al. (2017) simulated the tidal dynamics on the European Shelf with a range of SLR scenarios. And Pickering et al. (2017) extended the study to a global scale. They found that uniform SLR can lead to nonuniform tidal changes in space and the change is not proportional to SLR beyond a threshold. HWL events could further complicate the coupling of tidal dynamics and SLR. Horsburgh and Wilson (2007) used field observations to determine that storm surge increases the tidal water height by a small amount before and after the highest water peak. Lin et al. (2012) simulated clusters of hurricanes with sea level rise and found that the combined effect of storms, SLR, and tidal dynamics can significantly increase the flooding risk in New York city. In this study, we focus on high water events with time scales of days that are interacting with a tidal embayment, San Francisco Bay.

Geomorphology, particularly the shape and depth of a coastal basin, plays a dominant role in shaping the tidal dynamics. The seminal works of Parker (1984, 1991) developed a 1-D hydrodynamic model to analyze

Table 1
List of Simulation Configurations

Case	Shoreline scenario	Sea level (m)	Tidal boundary	HWL duration (day)
HWL2	Existing	0	No	2
HWL5	Existing	0	No	5
HWL10	Existing	0	No	10
HWL15	Existing	0	No	15
ExtLev	Existing	0	Yes	0
ExtLevHWL2	Existing	0	Yes	2
ExtLevHWL5	Existing	0	Yes	5
ExtLevHWL10	Existing	0	Yes	10
ExtLevHWL15	Existing	0	Yes	15
ExtLevRise	Existing	+0.5	Yes	0
ContainLev	Full-Bay containment	0	Yes	0
ContainLevHWL2	Full-Bay containment	0	Yes	2
ContainLevHWL5	Full-Bay containment	0	Yes	5
ContainLevHWL10	Full-Bay containment	0	Yes	10
ContainLevHWL15	Full-Bay containment	0	Yes	15
ContainLevRise	Full-Bay containment	+0.5	Yes	0

Note. Shoreline Scenario: "existing" refers to the present condition of the shoreline and "full-bay containment" refers to the complete containment construction following the shoreline. Sea level: rise of the mean sea level compared to the present condition. Tidal Boundary: whether tidal variation is enforced at the open boundary. HWL Duration: duration of the HWL event.

the generation of overtides and compound tides. Applying Fourier decomposition to the analytical model, he found that the nonlinear term in the continuity equation and the inertia term in the momentum equation are responsible for the even harmonic overtides, quarter diurnal, and terdiurnal compound tides, low-frequency compound tides, and the tide-induced change in the mean sea level. The friction term in the momentum equation contributes to the generation of odd harmonic overtides, semidiurnal compound tides, and other high-frequency compound tides. Friedrichs and Aubrey [1994] used a similar 1-D hydrodynamic model to study the estuaries that have exponential convergence. They concluded that the basin geometry can significantly change the tidal height spectrum.

Man-made infrastructure that is designed to protect the coastal community can change the geometry of the tidal basin, and in turn the tidal dynamics. At their extreme limits, the infrastructure projects can be categorized based on where they place their shorelines: "containment" refers to shorelines that are maintained at their current positions using constructed structures (levees, seawalls, or even restored marshes); "accommodation" refers to shorelines that are allowed to dynamically adjust as sea levels rise and new areas become inundated. Containment strategies are applied frequently in urbanized embayments, but the interplay of the tides with these shorelines may amplify tidal amplitudes and undermine local resilience by increasing the risks associated with catastrophic infrastructure failures and a reliance on supporting (pumping) infrastructure systems. Accommodation on the other hand, may improve local resilience by expanding tidal prisms horizontally, increasing frictional dissipation, and reducing the threats associated with infrastructure failures. Additionally, the return of tidal processes to these coastal areas renourishes ecosystems and improves water quality. Such restoration projects are increasingly being pursued in the United States and other developed countries where accommodation space is readily available. In spite of the advantages associated with accommodation approaches, they are rarely considered in urbanized regions.

The studies on the interaction between man-made infrastructure and tidal dynamics are relatively rare. Holleman and Stacey (2014) compared the tidal amplification before and after various scenarios of shoreline containment in San Francisco (SF) Bay, California. They simulated the tidal amplification with a monochromic tidal wave boundary (M_2 tide) using 1 m and half-meter projections of sea level rise. They found that at the south end of the bay, 1 m sea level rise with the current shoreline (i.e., a containment strategy) would increase the tidal amplitude by 33%, and a hypothetic full-bay containment would further increase the amplitude by 44%. This discovery is consistent with the observation in Pickering et al. (2017), who reported that more accommodation results in decreases of tidal amplitude after allowing increased flooding. Interestingly, Pelling and Green (2014) found the strongest tidal amplitudes happen with a partially protected

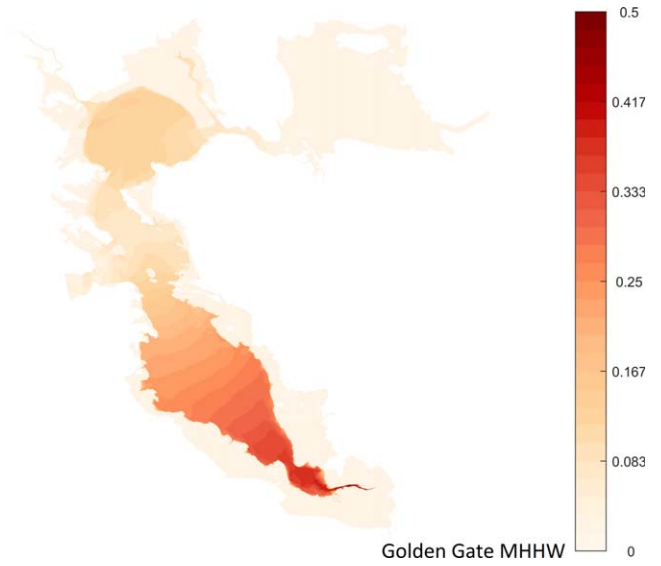

Figure 2. Mean higher high water (m) of Case ExtLev relative to the mouth of SF Bay at the Golden Gate.

coastline due to residual inland water and the interaction across events. Bertin et al. (2014) incorporated storm surge to the tide-coastal protection coupling system, and found that a seawall elevation to prevent storm flooding can raise the maximum water levels up to 1 m.

In the current work, we will pursue similar shoreline strategies to those in Holleman and Stacey (2014). Distinguishing this work from that previous work is our focus on a wide range of forcing frequencies, including the full tidal spectrum and an imposed perturbation ranging from a duration of 2 days to permanent (SLR) with a rise height of 0.5 m. Our focus, therefore, is on how this variety of forcing mechanisms interact to define high water levels in coastal embayments. To address the spatial and temporal complexity of the problem, analysis tools are needed to identify and visualize the key patterns within the complex dataset. Traditionally, researchers used Fourier Transform (FT) and Power Spectrum Analysis (PSA) to extract the tidal magnitude at different frequencies. More advanced data analysis tools were introduced in recent studies. For example, Castanedo et al. (2007) proposed to use a Kernel Density Function to represent the tidal height spectrum. Buschman et al. (2009) used regression models to fit the principal variations and explain them using the corresponding physical processes. Nidzieko (2010) and Song et al. (2011) used the skewness moment to quantify the tidal asymmetry. Sassi and Hoitink (2013) used the wavelet method to analyze the tidal amplitudes and phases. A recent method called Continuous Wavelet Spectrum (CWS) began to gain popularity among the scientific community (Guo et al., 2015; Jay et al., 2015). This method adds another dimension of time to the traditional wavelet analysis. Generally, these new methods focused on the characteristics in the time space and usually missed the spatial characteristics. To fill in this gap, we use a new tool, Dynamic Mode Decomposition (DMD), that can capture the coherent structure in space as well as in time. DMD was introduced by Schmid (2010) and originally developed to extract the coherent structure from turbulence. This tool can capture the coherent spatial structure at fixed frequencies such that both the time and spatial variation pattern can be simultaneously captured. The present paper will show that this tool is useful to analyze the tidal dynamics and to reveal hidden patterns that are difficult to retrieve with previously used methods.

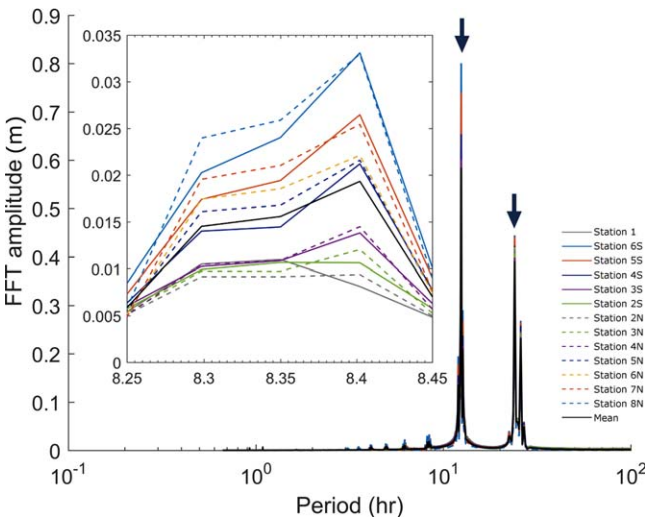

Figure 3. Tidal dynamics in SF Bay. The Fourier transform of the water level signal at the locations indicated in the inset map for Case ExtLev. Numbers in legend correspond to numbered locations on the map. The arrows point to the selected representative frequencies. The inset figure is a zoom-in of the overtide constituent.

2. Study Site

San Francisco Bay (SF Bay) consists of four tidal basins including South SF Bay (SSFB), Central Bay (CB), San Pablo Bay (SPB), and Suisun Bay (SB) (Figure 1). Golden Gate Strait connects SF Bay and the Pacific Ocean. This strait is 100 m deep and has mixed tides dominated by semidiurnal and diurnal constituents. SF Bay is strongly tidal, with tidal amplitudes as high as 1.5 m at the mouth and as much as 60% larger in the interior of the Bay. The major freshwater discharges are the Sacramento and San Joaquin Rivers (Figure 1), which contribute up to 90% of the total freshwater influx (Elias & Hansen, 2013).

South San Francisco Bay's shoreline has been extensively altered through the construction of levees around most of its perimeter, leading to a narrowing cross section with distance along the Bay's axis. A deep central channel extends the length of SSFB and has a depth of 12–20 m. The rest of the bay is a shallow basin, ranging from 5 m depth to the intertidal plain. Tides in SSFB are close to a standing wave. The velocity phase leads the water level peak by ~75° (Holleman & Stacey, 2014).

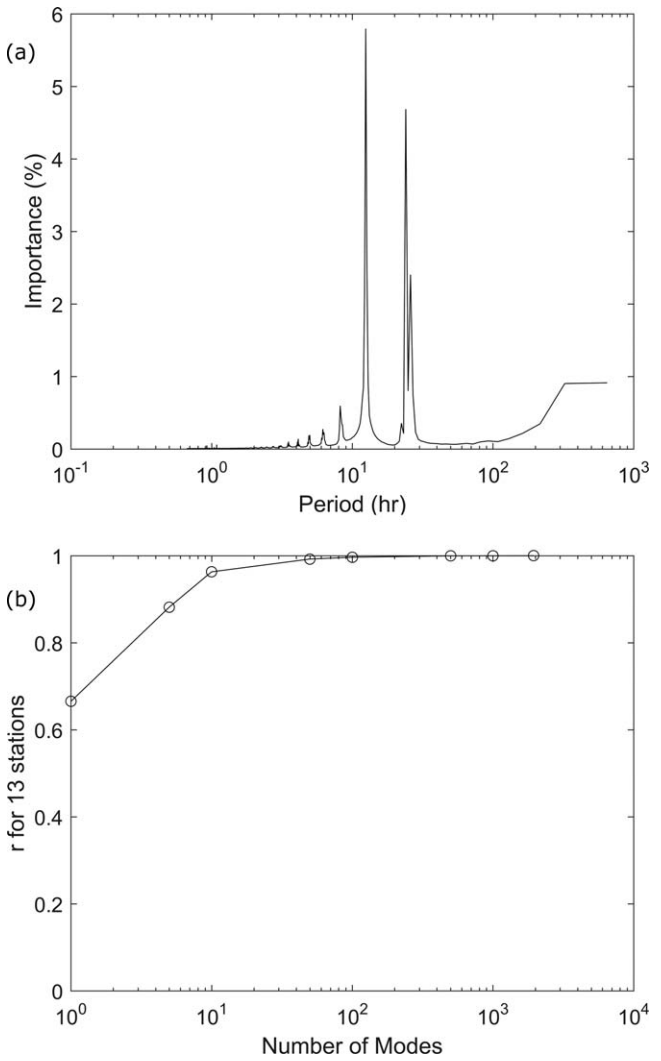

Figure 4. Holistic information of Case ExtLev generated by the Optimal DMD: (a) the importance of each mode by percentage, and (b) the share of the system by the modes.

The northern reach of SF Bay is a series of connected tidal basins, starting from Central Bay, to San Pablo Bay and Suisun Bay. The perimeter areas of San Pablo Bay and Suisun Bay were historically extensive tidal marshes, although much of that area is now separated from tidal action by levees or gates. Upstream of these basins lies the Sacramento-San Joaquin Delta, which is a network of channels that serve to effectively dissipate the incoming tidal wave, resulting in very little reflection along the axis of the northern reach of SF Bay. A deep channel is maintained through these basins and into the delta.

3. Methodology

3.1. Numerical Model

We used Delft3D Flow Flexible Mesh (D-Flow FM) to simulate the tidal dynamics of SF Bay (Deltares, 2016]. This software solves the shallow-water equation using an unstructured grid. The present paper employed a depth-integrated 2-D grid that was developed and shown reliable through a series of studies, including Elias and Hansen (2013), Erikson et al. (2013), and Martyr-Koller et al. (2017). We further increased the resolution up to the scale of 50 m close to the shoreline, allowing us to more accurately resolve the coastal infrastructure and other flood-control features. Updated shorefront topography was added following a recently released database of Doehring et al. (2016). Levee structures were simulated using the empirical "fixed weir" model described in the manual of D-Flow FM (Deltares, 2016). This model inserts a flow barrier at the specified location and the geometry of the domain and the momentum transport in the neighboring cells is adjusted using nonlinear empirical models.

An open boundary condition was applied outside of the Golden Gate. The north and south sides of the boundary were specified using the tidal constituents at Point Arena and Monterey respectively (NOAA, 2016). The west side was specified by a linear interpolation between these two sites, and was located ~70 km into Pacific Ocean. By comparison, the interpolated boundary condition is close to the tidal level prediction given by TPXO 7.2 (Egbert et al., 1994). A detailed comparison can be found in Appendix B. The model included 11 river discharges imposed at the numbered locations in Figure 1. The flow rate time series was obtained from the United States Geological Survey gauging sites (USGS, 2016). A drying and wetting numerical scheme was applied to the intertidal region.

The grid was partitioned into 28 parts. MPICH code was used to conduct the parallel computing on a 40 core workstation. A model validation showed that the present numerical model can reproduce the tidal water level with a correlation coefficient higher than 0.98 (see Appendix A for more details).

3.2. Configuration of Test Cases

We designed 16 numerical simulations with various shoreline configurations and tidal variability to investigate the interaction among the natural tides, HWL events, and infrastructure (Table 1). The first four cases, HWLx, were created to examine the tidal response of SF Bay to the top-hat water-rise events with different duration, which were imposed with a rise height of 0.5 m at the ocean boundary. Theoretically, such events can be expressed by

$$\eta = H(t-t_0) - H(t-t_e), \tag{1}$$

where t_0 and t_e are the starting and ending time of the HWL event, η is the normalized water level, and $H(x)$ is the Heaviside step function. Taking Fourier Transform, we obtain

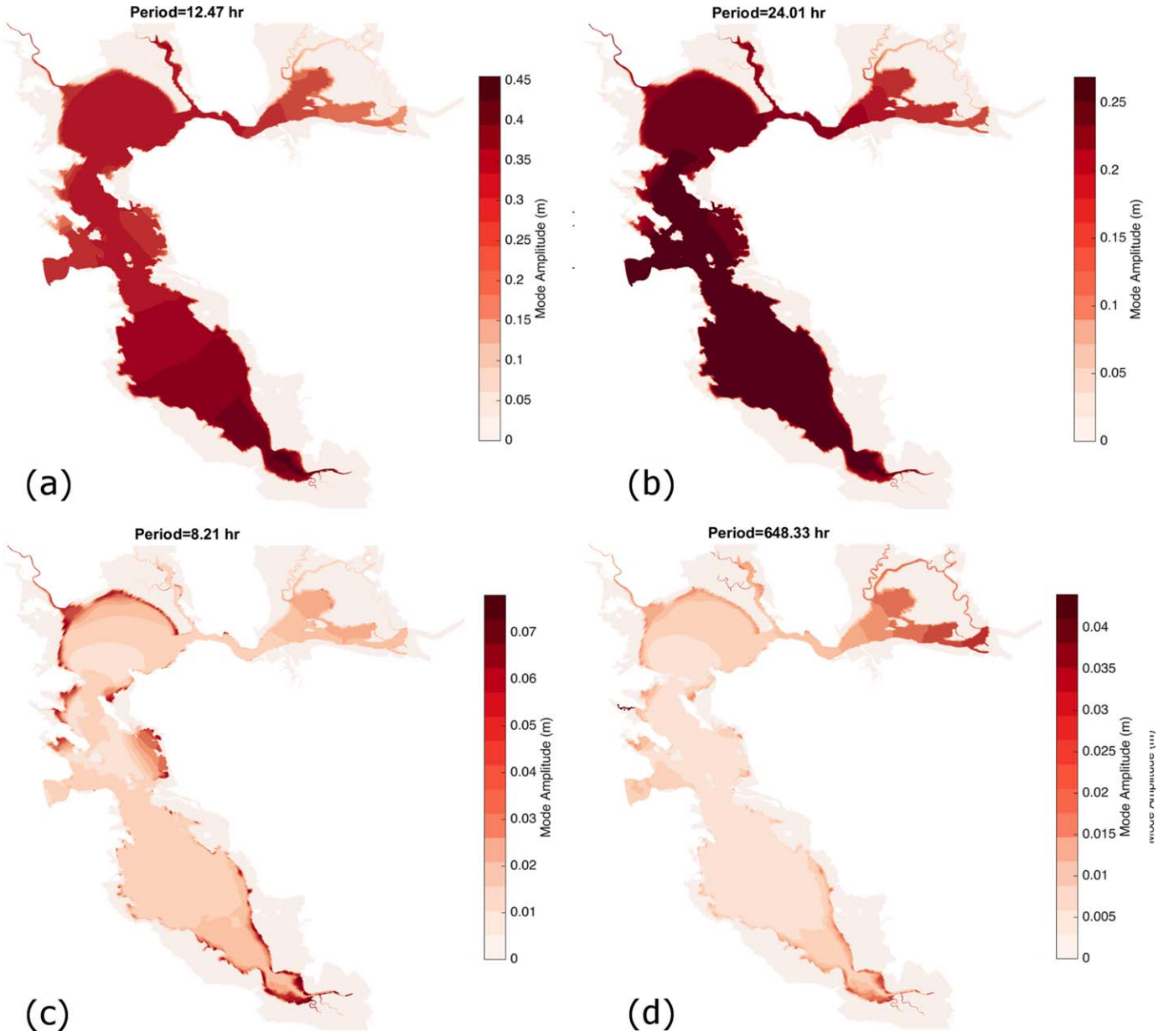

Figure 5. The results of Dynamic Mode Decomposition Modes for the existing shoreline scenario, i.e., Case ExtLev. The first three figures are corresponding to the selected frequencies in Figure 3.

$$\hat{\eta} = \sqrt{\frac{2}{\pi}} \frac{\left|\sin\left(\frac{t_e - t_0}{2}\omega\right)\right|}{\omega}, \tag{2}$$

where ω is the frequency. The limits of this equation are

$$\lim_{\omega \to 0} \hat{\eta} = \frac{t_e - t_0}{\sqrt{2\pi}} \quad \text{and} \quad \lim_{\omega \to \infty} \hat{\eta} = 0, \tag{3}$$

which outlines the magnitude and the shape of the spectrum. In general, the spectrum is a periodically decaying cascade toward high frequencies. A smoothing period of 4 h was used to remove the numerical singularity problem of the top-hat shape. Note that a case with a 2 h smoothing period was also compared and no obvious difference was observed, which proves that the smoothing period has no significant impact on the final results (see Appendix B for more details).

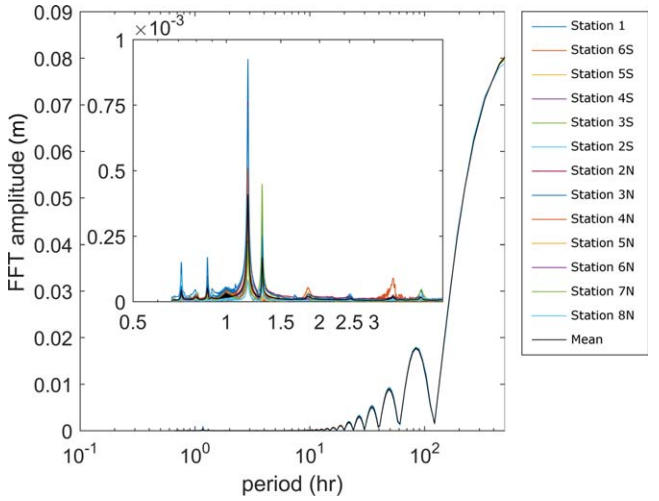

Figure 6. FFT spectra of the tidal water level of Case HWL5 at the 13 locations shown in the map in Figure 1. The inset shows the same spectra but of shorter periods.

Case ExtLev was created to reproduce the natural tidal dynamics with the existing shoreline configuration in SF Bay. Cases ExtLevHWLx were created by superimposing the open boundary condition of HWLx to ExtLev cases to check the interaction between astronomical tides and top-hat water-rise events. In these cases, the high water events flow over the existing levee structures and inundate perimeter lands. In the last six cases of ContainHWLx, we replaced the existing shoreline and seawall configuration by a full-bay containment that follows the land boundary in order to study the impact of infrastructure. The top-hat signal was added such that the perturbation was centered on the time of the highest water level (~4 P.M. on 12 January 2010) of the neap-spring cycle. The SLR case was created by adding a constant water elevation of half-meter to Case ExtLev. The present study assumed that the tidal amplitudes remain regardless of SLR scenarios. This assumption is supported by the global study of Pickering et al. (2017), which reported that the tidal amplitude on the west coast of the United States is subject to little change after SLR.

The shoreline configuration of Contain was created by replacing the existing topography with a full-bay containment, i.e., a continuous and infinite-height seawall following the coastline in the inset of Figure 3. In addition, we kept the major discharge of Sacramento and San Joaquin Rivers, but removed other freshwater discharge to avoid freshwater accumulation behind the hypothetical seawall.

3.3. Computing Dynamic Mode Decomposition (DMD)

Dynamic Mode Decomposition (DMD) is a Model Order Reduction (MOR) technique to extract spatial modes from dynamic systems (Schmid, 2010). Each DMD mode has a fixed frequency and growth rate. In comparison, the well-known Principal Orthogonal Decomposition (POD, also known as Empirical Mode Decomposition or Principle Component Analysis) extracts modes according to spatial variation. Each POD mode may involve multiple processes, potentially making it difficult to interpret the underlying physical processes. DMD was originally developed to recognize coherent structures from turbulent flows and has been applied to other fields, including flow-structure interaction (Gallardo et al., 2014), robotics (Berger et al., 2015), disease modeling (Proctor & Eckhoff, 2015), and Neural Activity Detection (Brunton et al., 2016). Following is a brief introduction of the DMD algorithm with an explanation of its application in tidal dynamics. To our knowledge, the present paper is the first study to introduce DMD to coastal tidal oceanography.

A typical case of our simulation contains a time series of water level at 200,103 grid elements and covers a 59 day period of 1 January to 28 February 2010 with an output time step of $\Delta t = 20$ min. Focusing on the tidal dynamics, we excluded Pacific Ocean and the intertidal region of the domain and removed the spin-up time of the first 3 days. Then, we derived a dataset of $n = 121{,}302$ grid elements and $m = 4{,}033$ snapshots. A snapshot at time $k\Delta t$ is denoted as a column vector $\vec{x}_k$. All the snapshots could be reorganized into two $n \times (m-1)$ data matrices,

$$X_t = \begin{bmatrix} | & | & & | \\ \vec{x}_1 & \vec{x}_2 & \cdots & \vec{x}_{m-1} \\ | & | & & | \end{bmatrix} \quad \text{and} \quad X_{t+1} = \begin{bmatrix} | & | & & | \\ \vec{x}_2 & \vec{x}_3 & \cdots & \vec{x}_m \\ | & | & & | \end{bmatrix}, \tag{4}$$

so that X_{t+1} is a one time step shift of X_t. Assume a linear operator A exists such that

$$X_{t+1} \approx AX_t. \tag{5}$$

Here A can be seen as a linear regression of the nonlinear dynamics of the system relating X_t and X_{t+1}. Perform the Single Value Decomposition (SVD) (Chatterjee, 2004),

$$X_t = U\Sigma V^T, \tag{6}$$

so we obtain A by the pseudoinversion

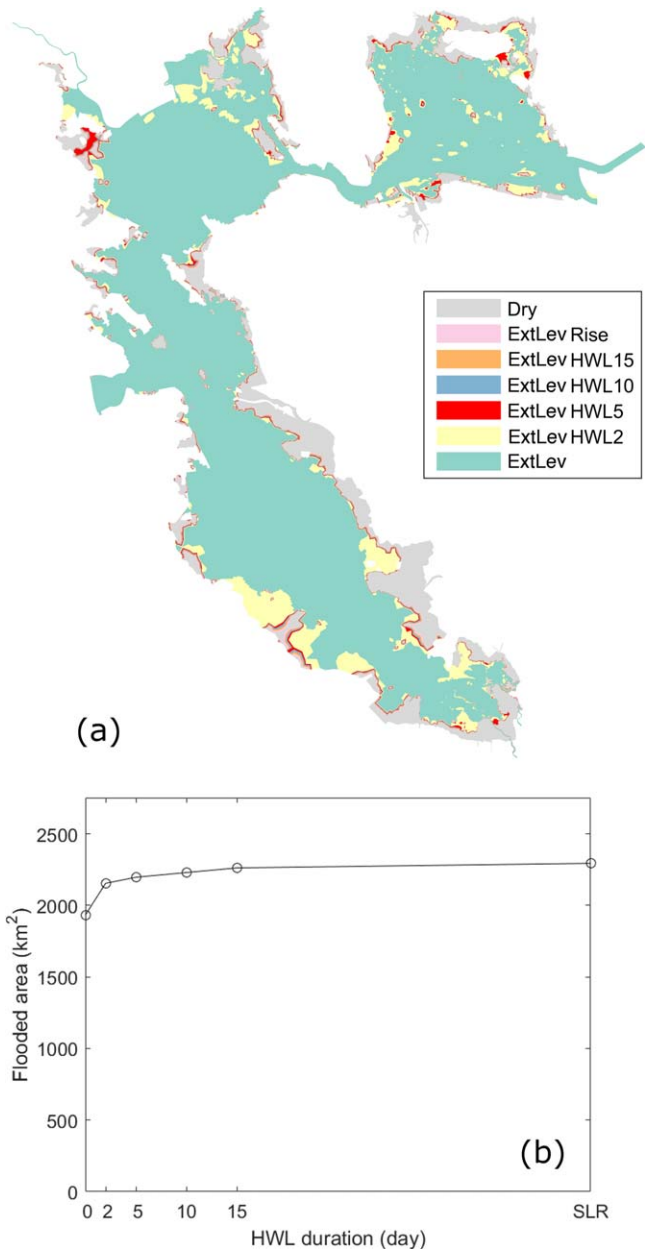

Figure 7. The flooding extents of different cases. (a) A map of SF Bay (37.40°N–38.29°N and 122.48°W–123.22°W) with colors showing the flooding extent for the case names indicated in the legend. Note that for high water events of duration longer than 5 days, the inundation does not extend beyond the area identified by the 5 day event; (b) The total area flooded versus the duration of the high-water-level event.

$$A = X_{t+1} V \Sigma^{-1} U^T, \tag{7}$$

where U is an $n \times n$ unitary matrix and V is an $m \times m$ unitary matrix. To get rid of the residue in the assumption of equation (5), a similarity transform was conducted

$$S = U^T A U = U^T X_{t+1} V \Sigma^{-1}. \tag{8}$$

Next, we performed the eigen decomposition for the matrix S

$$SW = W\Lambda, \tag{9}$$

where W is the matrix of eigenvectors, and Λ is the diagonal matrix of the eigenvalues λ_i. Finally, the DMD modes could be recovered by the similarity transform

$$\Phi = UW, \tag{10}$$

where the columns of Φ are the DMD modes, which define the spatial structure of the mode, and the real and imaginary parts of the eigenvalues in Λ indicate the stability and the frequency of each mode, respectively. For periodic data, the growth rate would be expected to be zero so that purely imaginary eigenvalues would emerge with the frequency content of the input data. More details about the algorithm can be found in Schmid (2010).

Because of the involved eigen decomposition, DMD is developed to generate normalized modes that cannot reflect the magnitude of the original dynamics. Chen et al. (2012) resolved this problem by projecting the derived modes back to the original data. After solving a convex optimization problem, the importance of each mode can be obtained (Jovanović et al., 2014), using

$$\alpha = \left((W'W) \cdot \left(\overline{V_{and} V_{and}^*} \right) \right)^{-1} \overline{diag(V_{and} V \Sigma^* W)}, \tag{11}$$

where V_{and} is the Vandermonde matrix, i.e.,

$$V_{and} = \begin{bmatrix} 1 & \mu_1 & \cdots & \mu_1^{m-1} \\ 1 & \mu_2 & \cdots & \mu_2^{m-1} \\ \vdots & \vdots & \ddots & \vdots \\ 1 & \mu_n & \cdots & \mu_n^{m-1} \end{bmatrix}, \tag{12}$$

the asterisk sign denotes the complex-conjugate-transpose of a vector or a matrix, the overbar denotes the complex-conjugate matrix, $diag(X)$ is a vector determined by the main diagonal of a given matrix, X, and μ is the diagonal element of Λ. The new method is named as Optimal DMD so that the DMD modes can be scaled up using the importance vector α (Jovanović et al., 2014).

DMD has three features in comparison with Fourier Transform. First, DMD can estimate the importance of each mode, giving a summary of the importance of different frequencies in the dynamic system, whereas FFT has to be applied to individual points, which will miss the more holistic picture of DMD. Second, DMD can help build a reduced-order model to predict the system dynamics without running the full-scale model. Third, DMD is able to estimate the stability of each mode. For our purposes, in a tidally dominated system, the process is periodic and every mode has a zero growth/decay rate in the present study, so the results from the DMD are similar to a point-by-point Fourier transform analysis throughout the domain. The added value of DMD that lies in the growth rates of modes is not important for this case.

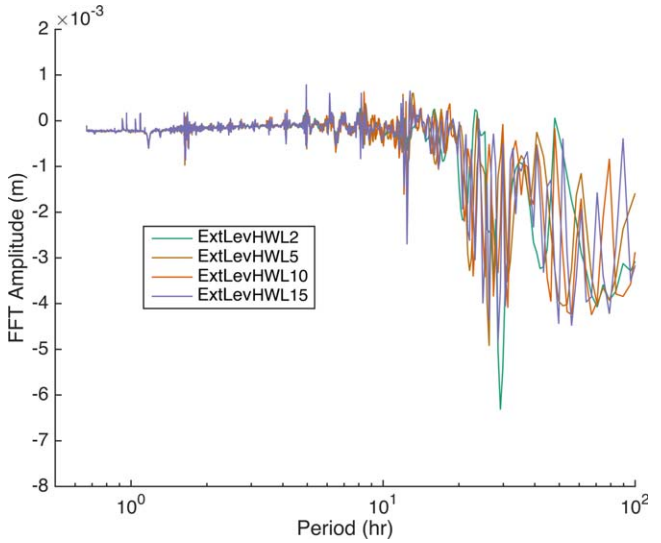

Figure 8. FFT spectrum of the difference between ExtLev and each HWL event ($h_{ExtLevHWLx} - h_{ExtLev}$) for existing shorelines.

4. Results

4.1. Tidal Dynamics and Flooding

Figure 2 shows the relative Mean Higher High Water (MHHW) of Case ExtLev using Golden Gate as the reference, where MHHW is calculated by averaging the daily highest water level peaks at each grid point. This figure shows that the south end of SSFB and the middle of SPB have local MHHW maxima. Their heights of ∼0.5 and ∼0.2 m are consistent with the M_2-driven simulations by Holleman and Stacey (2014). This consistency indicates that the tidal constituent of *M*2 dominates the MHHW of SF Bay.

We sampled the water level at 13 stations from all of the tidal basins. Their Fast Fourier Transform (FFT) are shown in Figure 3 and their locations are specified in the inset. The spectral shape of the tidal height is similar at all the stations. The highest two peaks are the semidiurnal and the diurnal constituents, which are driven by the astronomical forcing. Note that a second peak with a slightly longer period exists next to the diurnal peak. A cascade of short-period peaks appear at the overtide frequencies, i.e., 8 h, 6 h, and so on. From the inset figure, we can see that overtide is stronger if the location is further into the bay. This is due to the nonlinear processes inside the bay that are stronger with shallower waters.

Figure 4a shows the importance of each mode for the frequency of the process. The distribution is similar to the shape of FFT in Figure 3, except the relatively greater importance in the long-period modes. This difference indicates that Optimal DMD is more sensitive to the low-frequency processes than FFT. The importance spectrum shows the relative importance of each mode and can be used to develop a reduced-order model. For example, picking the modes with leading importance, we could reconstruct the water level of the whole domain. The accuracy of the reduced-order model can be shown using Pearson correlation coefficient, *r*. Figure 4b compared prediction of the water level at 13 stations between the reduced-order model with different number of modes and the original simulation results. The comparison shows that with the first leading mode, the reduced-order model can reproduce the water level with $r = 0.67$, and r rises to 0.96 with the first 10 leading modes. This comparison demonstrates the potential to use Optimal DMD as a model order reduction tool in coastal hydrodynamics.

We selected four representative DMD modes according to the highest, second highest, third highest peaks of Figure 3, and a low-frequency mode. They are shown in Figure 5, exhibiting the spatial patterns of the natural tidal dynamics. Corresponding to the highest peak of Figure 3, the representative semidiurnal constituent with the period of 12.47 h (Figure 5a) has a high amplitude at the south end of SSFB and a local maximum at the center of SPB. This pattern is similar to the MHHW of Figure 2. In comparison, the representative diurnal constituent with the period of 24.01 h (Figure 5b), corresponding to the second highest peak of Figure 3, has a relatively uniform height in SSFB and a slope in SPB and SB. This pattern indicates a longer wavelength compared to the semidiurnal one. The first overtide mode (Figure 5c), corresponding to the third highest peak, has an increased height surrounding the coastline, which is expected due to its dependence on nonlinear processes that are strongest in shallow waters. Finally, the long-period mode (Figure 5d), which is likely dominated in these simulations by river flow as modulated by the spring-neap cycle, has higher amplitude near the coast, but also shows increases along the northern and southern axes of the Bay. In general, we observed that modes with similar periods share a similar pattern; thus the selected modes shown can represent their neighbors in frequency space.

4.2. High-Water-Level (HWL) Events

The spectra of the tidal water level at 13 locations specified by the inset of Figure 1 are shown in Figure 6. The trend of the spectra follows equation (2), but a difference is noted at very short periods (∼1.3 h; inset of the figure). This difference can be interpreted as the surface seiche period for the basin. Assuming SF Bay can be approximated as a simple closed basin, we can calculate the seiching period using the Merian formula for a rectangular basin (Proudman, 1953),

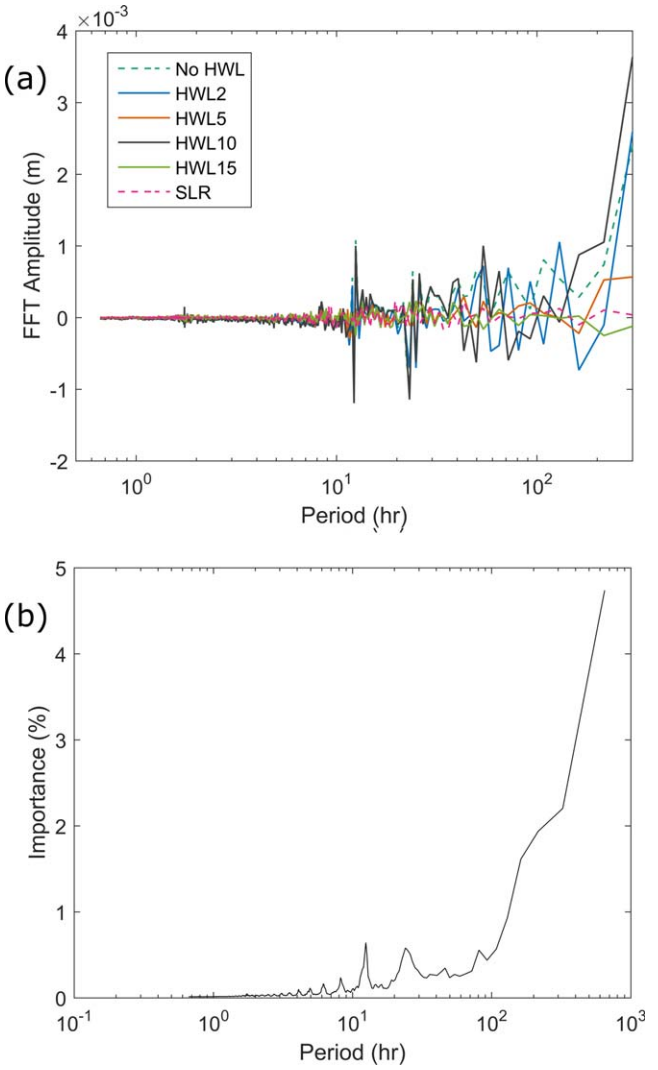

Figure 9. Overview of the information between ExtLev and ContainLev generated by the Optimal DMD: (a) the importance of each mode by percentage ($h_{ContainLevHWLx} - h_{ExtLevHWLx}$), and (b) the difference in the share of the system by the modes ($h_{ContainLevHWL2} - h_{ExtLevHWL2}$).

$$T = \frac{2L_{sf}}{n\sqrt{gh_{ave}}}, \tag{13}$$

where L_{sf} is the length of the basin, h_{ave} is the average depth of the basin, and n is the number of nodes. For basins with horizontal scales 20–50 km (representative of the subbasins in SF Bay) and average depths of 8–12 m (representative of the deep channels in each basin), the first mode ($n = 1$) would have a period of 1–3 h.

Adding the top-hat signal to Case ExtLev, we studied the interaction between HWL events and the astronomical tides of SF Bay. The flooding extent, which is the area flooded by at least 1 cm, is shown in Figure 7a. This figure shows that the presence of the HWL events extends the flooding extent. And the longer the HWL event lasts, the greater the flooding extent spreads. This trend is quantified in Figure 7b, and the trend can be divided into two stages. Before the duration of 5 days, the flooding extent increases quickly, while afterward the flooding extent stays relatively stable and is close to the sea level rise (SLR) case.

Figure 8 shows the residual FFT spectra after subtracting the spectra of ExtLev and the corresponding HWLx from ExtLevHWLx for the average of the 13 stations. These residual spectra represent the nonlinear interaction between the top-hat sea level rise and the astronomical constituents. We found the nonlinear interaction between these components is only ~1% of the original spectrum, so the FFT spectrum of ExtLevHWLx can be approximated as the linear superposition of Cases ExtLev and HWLx. An oscillation was observed at the low frequencies, which indicates that nonlinear interactions reduce the low-frequency tidal constituents.

4.3. Infrastructure

The difference of the 13 station average spectrum between ExtLevHWLx and ContainHWLx shows the impact of the full-bay containment (Figure 9a). The figure shows that the full-bay containment can change the tidal dynamics up to 5% and the impact is concentrated in the low frequencies. This result is also reflected in the importance spectrum generated by the Optimal DMD shown in Figure 9b.

The impact of the full-bay containment in space can be seen in the DMD modes of Figure 10. These modes are generated by analyzing the water level difference between Case ExtLev from Contain. The semidiurnal mode (Figure 10a) has high amplitudes at the shoreline of San Pablo Bay and the south end of South San Francisco Bay. This observation shows that the coastal protection infrastructure changes the nearby region the most. In the diurnal mode (Figure 10b), the impact of the seawalls extended into the bay due to the longer wavelength in this frequency. Figure 10c shows the impact in the overtide mode, in which Central Bay and South San Francisco Bay have many oscillations. This variability reflects the complicated distribution of the nonlinear effects induced by the seawall protection. The long-term tidal mode shown in Figure 10d is indicating a universal change in space. So the most important impact of the full-bay containment is in the long-term process, which is fairly uniform in space.

4.4. Analysis of the Dispersion of HWL Events

The mechanism of dispersion can be evaluated by comparing the water level time series between mouth and locations inside the bay. We subtracted Case ExtLev from ExtLevHWLx to focus on the change by the top-hat signal. The mouth (Golden Gate site) and the interior (Port Chicago site) are compared in Figure 11. It is clear that all the HWL events reach the same peak height of the water level at the Golden Gate. However, the peak water level of HWL2 is lower than the other cases in Port Chicago. This reduction is due to

the dispersion of the HWL event within the bay such that the maximum of the top-hat signal is reduced. For HWL events of 5 or more days, the maximum is comparable across all cases, which indicates that SF Bay is only able to disperse events of duration shorter than this threshold. This threshold will vary in other coastal embayments, but is easily evaluated with a limited set of simulations.

Figure 12 shows the dispersion process of a 2 day top-hat HWL event with the existing shoreline scenario. The water level results are obtained by subtracting the results of ExtLev from ExtLevHWL2. The water level at the open boundary, i.e., the site of Point Arena, follows a smoothed top-hat profile. The profile inside the bay, i.e., at Site 8N (Figure 1), becomes wider and lower than the former with a horizontal shift.

4.5. A 1-D Inverse Modeling Analysis of HWL Events

Based on the shallow-water equations, a 1-D open channel flow can be developed following the diffusion wave model of "flood routing" in Henderson (1996):

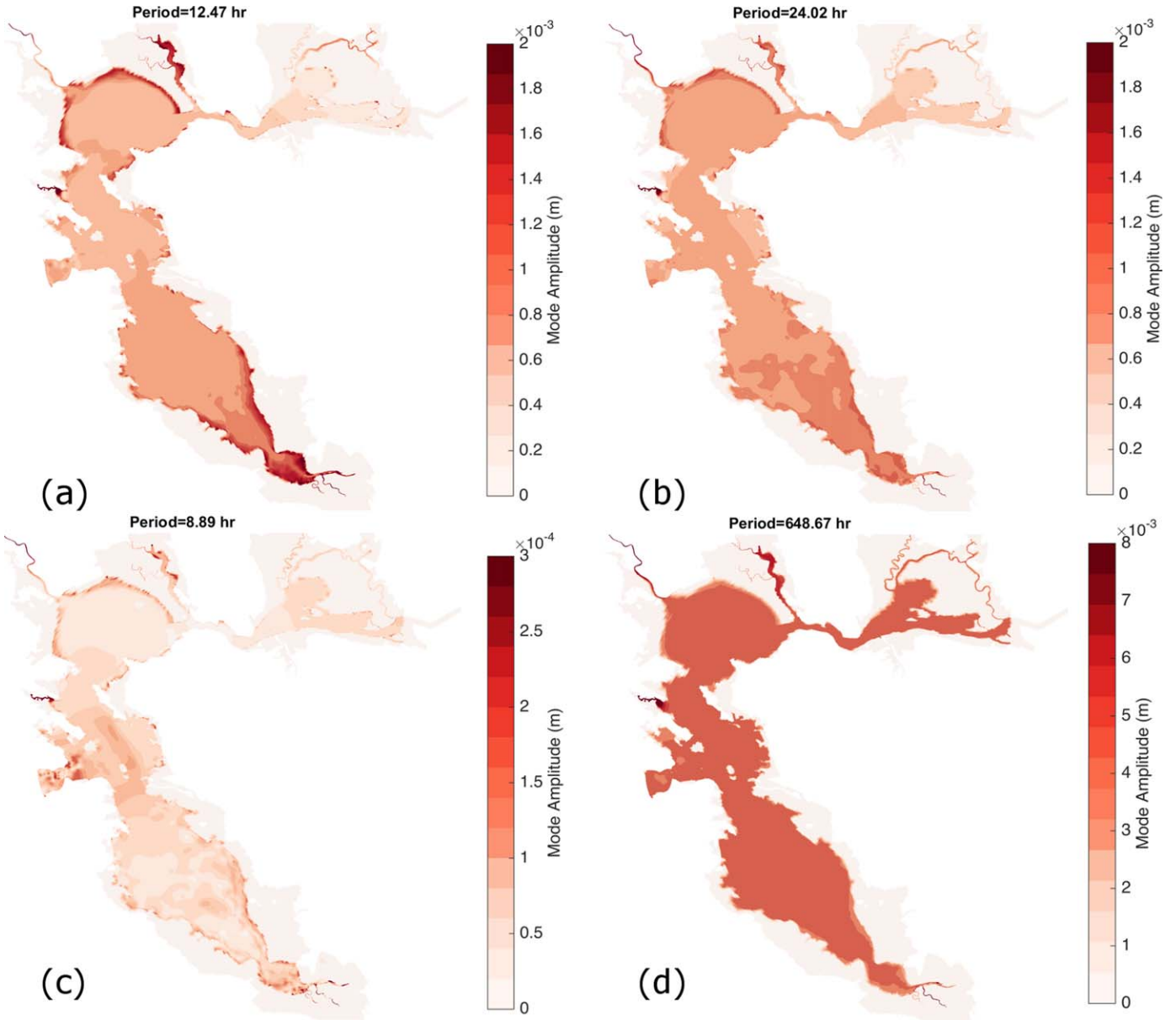

Figure 10. DMD Modes of the difference between ExtLev and ContainLev ($h_{ContainLev} - h_{ExtLev}$).

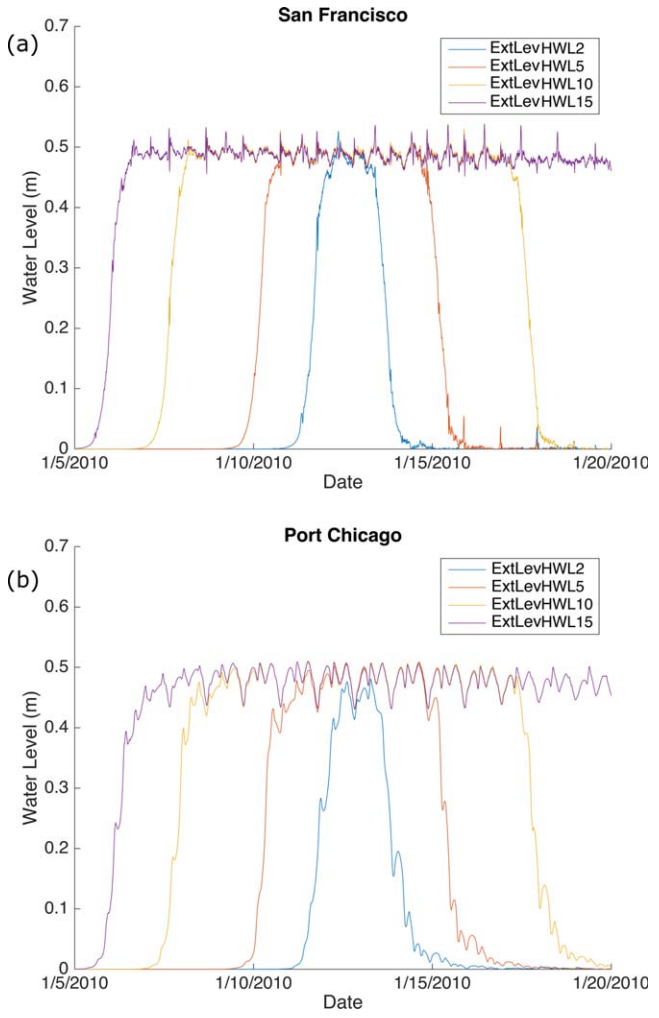

Figure 11. Modeled water levels ($h_{ExtLevHWLx} - h_{ExtLev}$) for different duration high-water-level events in (a) San Francisco and (b) Port Chicago.

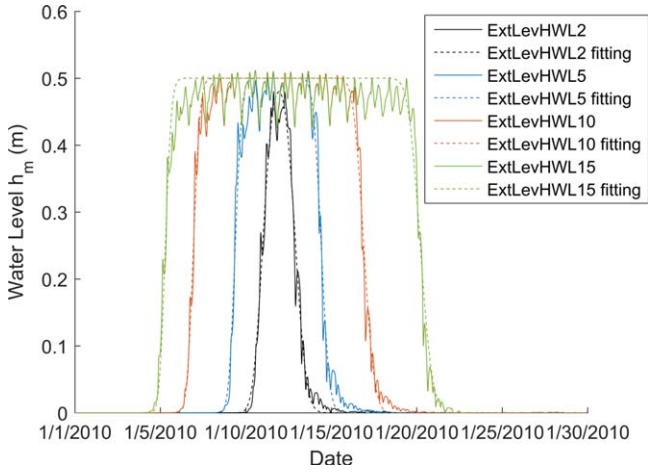

Figure 12. Modeled water levels at site 8°N (Figure 1). The fitting model shows a good quality to compare with the diffusion model described in the text.

$$\frac{\partial h}{\partial t} + C\frac{\partial h}{\partial x} = D\frac{\partial^2 h}{\partial x^2}, \tag{14}$$

where h is the water level, t is time, x is spatial coordinate, C is the group velocity, and D is the pseudo diffusion coefficient. Note that "dispersion" might be a more appropriate term in physics to describe the profile change between Point Arena and a site in the interior of the Bay, but mathematically the process can be approximated as a process of "diffusion" quantified by the diffusion coefficient of "D." The top-hat initial condition is

$$\frac{h}{h_0} = H(x - x_0 - L) - H(x - x_0) \tag{15}$$

and the boundary condition is

$$h(-\inf, t) = 0 \quad and \quad h(\inf, t) = 0, \tag{16}$$

where h_0, L, and x_0 are the height, length, and starting point of the initial top-hat profile, and $H(x)$ is the Heaviside function. An analytical solution can be derived assuming C and D are constants,

$$\frac{h}{h_0} = \frac{1}{2}\left[erf\left(\frac{x - x_0 - Ct}{\sqrt{4Dt}}\right) - erf\left(\frac{x - x_0 - C(t+\Delta t)}{\sqrt{4Dt}}\right)\right]. \tag{17}$$

At an observation point on the spatial coordinate, e.g., x_s, the time series solution is

$$\frac{h_m}{h_0} = \frac{1}{2}\left[erf\left(\frac{x_{s0} - Ct}{\sqrt{4Dt}}\right) - erf\left(\frac{x_{s0} - C(t+\Delta t)}{\sqrt{4Dt}}\right)\right], \tag{18}$$

where $x_{s0} = x_s - x_0$.

This 1-D model captures the translating and diffusing processes observed in Figure 12. The model involved four unknowns including C, D, L, and x_{s0}, which can be determined using inverse methods for all the cases in order to quantify the impact of the astronomical tidal constituents and the coastal infrastructure. Assuming the initial profile is a half-meter top-hat, we minimize the objective function:

$$J = |h_s - h_m|_2, \tag{19}$$

which is the two norm of the difference between the full-scale simulation results (h_s) and the 1-D model (h_m) at Site 8N (Figure 1). This unconstrained minimization problem is solved using MATLAB. Note that we have to assign a value to the advection speed (we chose $C = 7$ m/s, which corresponds to an average water depth of 5 m) to ensure the problem has a definite result, otherwise any combination of the four unknowns that share the same ratio in the error functions would lead to the same minimization result. In another words, the determined unknown can be scaled with a factor to minimize equation (19). As an example, the best fitting 1-D model solutions for the demonstration cases are shown in Figure 12.

Table 2 lists the determined D, which provides a comparison of the effective diffusion coefficients for all the cases. It is clear that the dominant factor in determining the diffusion of a high water event is the presence of tidal motions and that the duration of the high water event itself has a significant impact but in an order of magnitude smaller than the effect of tide. The values in Table 2 demonstrate that tidal motions increase the effective diffusion coefficient by a factor of

Table 2
List of the Effective Diffusion Coefficient of the 1-D Diffusion Wave Model Determined by the Inverse Method Between the Pacific Ocean Boundary and Site 8N° (Figure 1)

Case	Duration (day)	D ($\times 10^4$ m^2/s)
ExtLevHWL2	2	4.29
ExtLevHWL5	5	2.48
ExtLevHWL10	10	5.88
ExtLevHWL15	15	4.16
ContainLevHWL2	2	4.30
ContainLevHWL5	5	2.47
ContainLevHWL10	10	5.84
ContainLevHWL15	15	4.32
HWL2	2	0.71
HWL5	5	0.82
HWL10	10	1.14
HWL15	15	0.75
ExtLevHalfRoughness	2	7.93
ExtLevDoubleRoughness	2	2.49

4–6. Additional simulations were performed to investigate the effect of bottom roughness. The Manning's roughness coefficient of a case was all doubled or halved to show the impact. We found that the influence of the tides is modulated by the bed roughness with inverse dependence on the Manning's roughness coefficient; if the roughness coefficient is doubled, the diffusion coefficient is reduced by about 40%, and if the roughness coefficient is halved, the diffusion coefficient is increased by about 85%. So, while the analysis above demonstrated that the presence of a multiday high water event does not significantly alter the tidal dynamics, the reverse is not true. Instead, tidal motions are the critical factor in establishing the diffusion (and dissipation) of multiday high water events.

The heterogeneity of the topography of SF Bay provides a test bed to examine the importance of the impact factors of roughness, geometry, and resonance in coastal dispersion process. The values of the effective diffusion coefficients in Table 2 represent the aggregated diffusion from the source (somewhere in the Pacific) to site 8N (Figure 1). Similar values are found at other locations along the Bay, but these values are all strongly influenced by the transition from the boundary into the Bay. In order to focus on local processes inside the Bay, we now convert these aggregated effective diffusion coefficients to local values, which are defined by the change in the effective diffusion coefficient between two stations based on the definition of the diffusion coefficient as one half of the rate of change of the variance. The variance is proportional to the diffusivity Dx/C, where C is the constant wave translating speed. We define $D_{i->j}$ as the equivalent diffusion coefficient such that the difference of the variance between two sites equals to the product of the distance between the two sites and $D_{i->j}$, i.e.,

$$\frac{D_{i->j}\left(x_{s_{0j}}-x_{s_{0i}}\right)}{C}=\frac{D_j x_{s_{0j}}}{C}-\frac{D_i x_{s_{0i}}}{C}, \tag{20}$$

where D_i is the aggregated effective diffusion coefficient at $x_{s_{0i}}$. x_{s0i} is the total distance from x_0 to Site i, which is determined in the inverse calculations. So $D_{i->j}$ represents the dispersion process from the down-estuary Site i to its up-estuary neighbor, j. It can be conveniently calculated by

$$D_{i->j}=\frac{D_j x_{s_{0j}}-D_i x_{s_{0i}}}{x_{s_{0j}}-x_{s_{0i}}}. \tag{21}$$

The resulting local diffusion coefficients are shown in Table 3 and Case ExtLevHWL2 is shown in Figure 13a.

Table 3
Local Diffusion Coefficient at the 13 Sites for Case ExtLevHWL2, ContainLevHWL2, and Their Difference ($h_{ContainLevHWL2}-h_{ExtLevHWL2}$)

i->j	ExtLevHWL2 D ($\times 10^4$ m^2/s)	ContainLevHWL2 D ($\times 10^4$ m^2/s)	Difference D ($\times 10^4$ m^2/s)
5°S->6°S	17.0	17.2	0.19
4°S->5°S	27.6	24.4	−3.21
3°S->4°S	30.6	26.6	−4.01
2°S->3°S	41.4	33.9	−7.54
1°S->2°S	10.9	2.1	−8.79
1°N->2°N	17.9	18.5	0.55
2°N->3°N	112.4	108.4	−3.96
3°N->4°N	152.9	149.0	−3.88
4°N->5°N	252.8	251.5	−1.28
5°N->6°N	256.7	248.2	−8.49
6°N->7°N	630.8	640.9	10.12
7°N->8°N	1145.3	1154.6	9.25

As the high water event enters the Bay, it travels to the north and to the south, diffusing as it progresses. In South San Francisco Bay, surprisingly, the local diffusion coefficient actually *decreases* toward the head of the Bay, in spite of the fact that the tidal amplitude increases. This result contradicts the conclusion that tidal dynamics dominated the effective aggregate diffusion coefficient, but now at a local scale, the details of how the tides disperse the high water event become more important. In this case, as the tidal amplitudes grow toward the head of the Bay, the available accommodation space on the perimeter of the Bay decreases as the Bay narrows. The result is that the higher tidal amplitudes in the far southern part of the Bay are actually *less* effective at diffusing the high water event because there are very limited perimeter volumes with which the tides can interact.

The reverse is true in North Bay, where the diffusion coefficient increases along the axis of the Bay, even though the tidal amplitude decreases between San Pablo Bay and Suisun Bay. Here again, the available accommodation volume is critical to defining the local

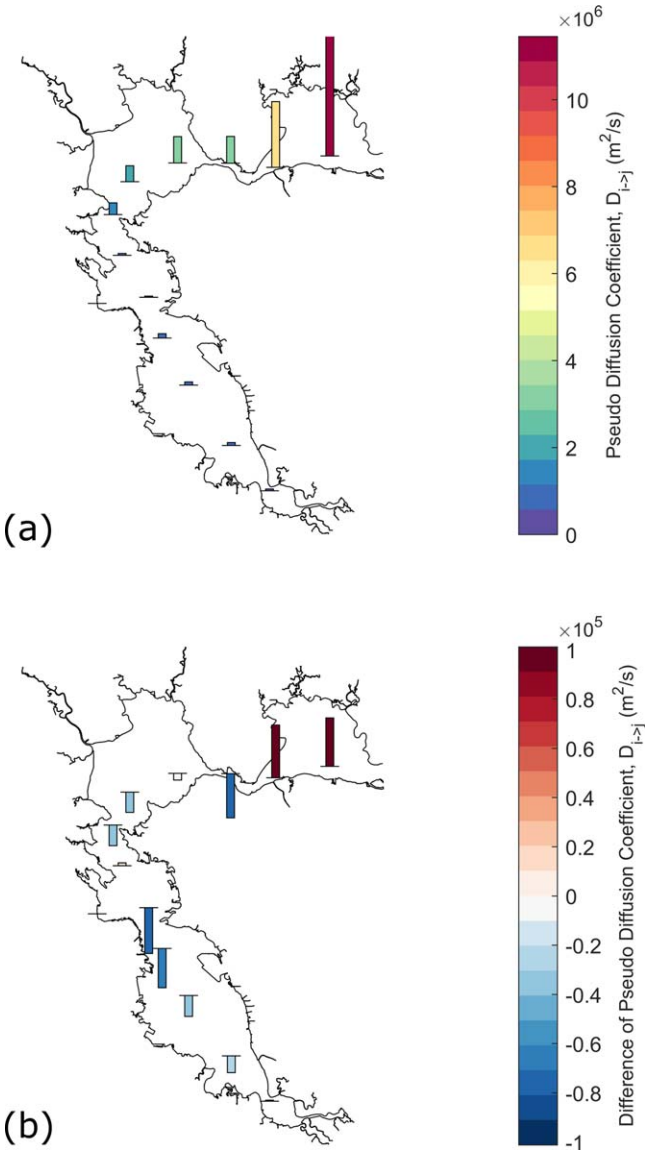

Figure 13. Local diffusion coefficient of the 13 sites calculated based on the difference between a site and its down-estuary neighbor. The height and color of the bar is proportional to (a) the local diffusion coefficient and (b) the difference of the diffusion coefficient between ExtLevHWL2 and ContainLevHWL2 ($h_{ContainLevHWL2} - h_{ExtLevHWL2}$, i.e., the effects of shoreline configuration on the diffusion of a 2 day high water event).

diffusion coefficient. In contrast to South Bay, extensive accommodation space is available on the perimeters of both San Pablo Bay and Suisun Bay, so that, even though tidal energy is reduced in the upper reaches of the estuary, the diffusion of a multiday high water event is enhanced through the interaction of the tidal oscillations and the high water event itself with the accommodation volume around the perimeter of the estuary. This result highlights the importance of the perimeter shorelines for the ability of an estuary to diffuse (or dissipate) a multiday high water event. It should be noted, however, that this same conclusion does not hold for long-term sea level rise, due to the fact that there is no "event" to be diffused in that case.

Finally, we explore how shoreline infrastructure strategies modify the diffusion of the multiday high water event. In Figure 13b, the difference between containment (ContainLevHWL2) and accommodation (ExtLevHWL2) is illustrated using the change in the local diffusion coefficient between the two cases. A negative value for this difference (also appearing in Table 3) indicates that the accommodation case has *greater* diffusion than the containment case. Throughout most of the Bay, except for the far northern embayment, Suisun Bay, we can see in Figure 13b that this difference is, in fact, negative, and providing "extra" accommodation space along the perimeter increases the ability of the embayment to diffuse a high water event. The only counter-examples to this conclusion are in Suisun Bay, where the accommodation strategy actually *decreases* the diffusion of a multiday high water event. The mechanism behind this counter-intuitive result is unclear, although we hypothesize that it may be due to a reduction in the tidal energy reaching Suisun Bay as a result of the extra accommodation along the axis of the Bay, which overwhelms the small change in accommodation volume within Suisun Bay itself (due to the fact that it has large accommodation volume in either case).

5. Discussion

Flooding area is determined by the amount of overtopping flow during the period of high water level. One would argue that the flooding extent only depends on the height and duration of the overwhelming water level regardless of the number of the water-rise events, because the water would retreat from the land during the low tide between the events and resets the flooding starting point. However, our study shows that the number of the events matters, because we observed greater flooding extents for the same magnitude but longer duration HWL events (Figure 7). Three possible mechanisms could potentially explain such increased flooding extent, including (1) the nonlinear interaction between the astronomical forcing and the HWL event, (2) the dispersion of the HWL event within the bay, and (3) the water residual left by previous floods.

As shown in our analysis, the influence of multiday events on the tidal dynamics is quite limited, so it is unlikely that the first mechanism is responsible. The one-dimensional diffusion model indicates that high water events are effectively diffused by tidal dynamics and perimeter accommodation volume, making it likely that the second mechanism is explanatory. It appears that, for San Francisco Bay, this mechanism is relevant to an event of duration 2–5 days; for events longer than that (including long-term sea level rise), the peak event is not reduced as it travels into the embayment. Any expansion of the flooded area for events longer than about 5 days is likely to be attributed to the cumulative effect of multiple flooding events, and the presence of residual waters from previous events. We checked the existence of such

Table A1
Comparisons of Water Levels for Validation

Station name	*r*	Lag (s)	RMS ratio
Point Arena	0.9996	−122	1.001
Monterey	0.9993	−120	0.986
San Francisco	0.9952	98	1.033
Alameda	0.9970	193	1.027
Richmond	0.9971	−433	1.017
Redwood City	0.9960	202	1.002
Coyote Creek	0.9923	−259	0.973
Port Chicago	0.9885	−530	1.052
Martinez	0.9862	−420	0.969

residual water level by picking the lowest tide of a day and compared it to the next day. The result shows that water was left by the flood of the previous day. The most residual water concentrates in the wetlands at the north and the south ends.

These results highlight the role that expanded shoreline accommodation, whether in the form of natural ecosystems (marshes) or floodable urban landscapes, can play as a buffer to high water events. While these accommodation spaces cannot dissipate long-term events, like sea level rise, they can play an important part in dissipating shorter events; in San Francisco Bay, even just allowing events to overtop existing levees provides protection against events with duration of 2 days.

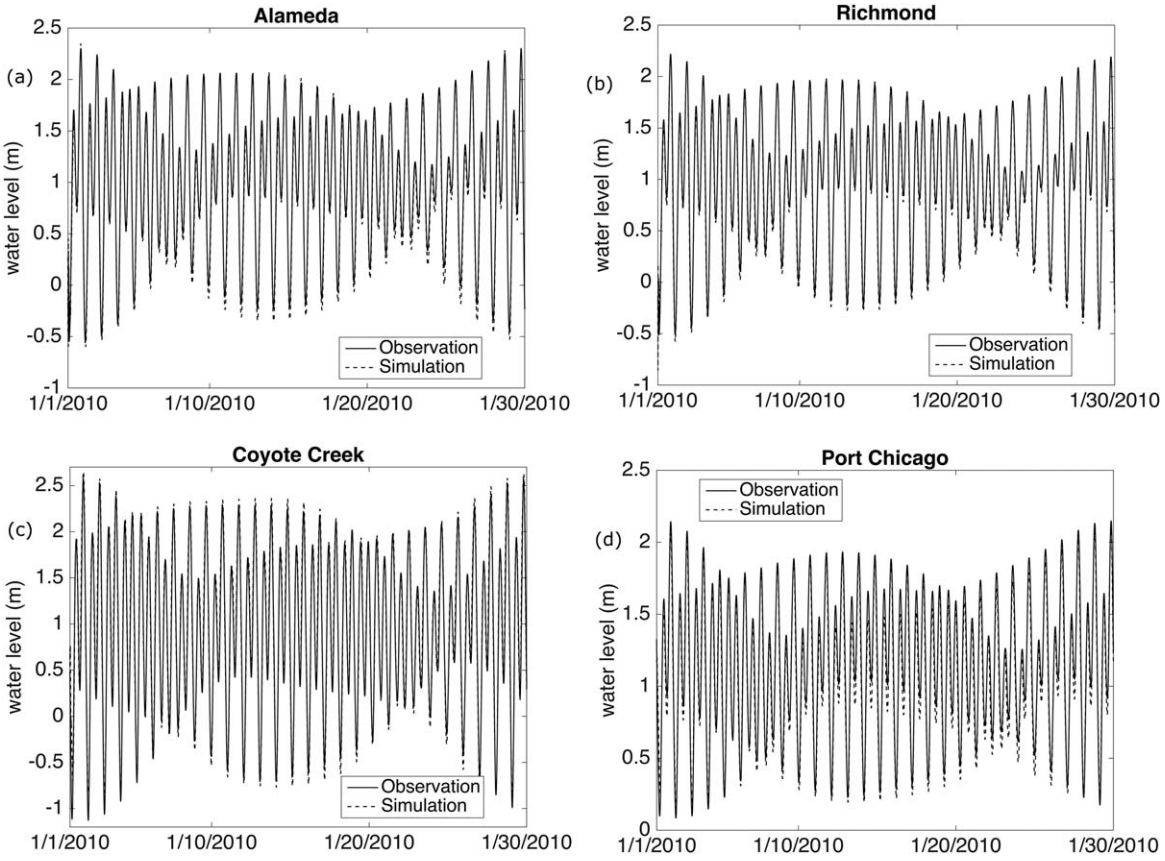

Figure A1. Comparison of observed and simulated water level at the sites of (a) Alameda, (b) Richmond, (c) Coyote Creek, and (d) Port Chicago.

Table B1
Comparisons of the Water Level at Eight Equally Distant Points Along the Open Ocean Boundary Between the Interpolated Boundary Condition and the one Generated by TPXO 7.2 (Egbert et al., 1994) to Show That There was no Significant Difference Between Them

Site number	*r*	RMS ratio
1	0.9962	0.9908
2	0.9954	0.9926
3	0.9954	0.9938
4	0.9966	0.9939
5	0.9970	0.9936
6	0.9969	0.9931
7	0.9973	0.9912
8	0.9964	0.9911

6. Conclusions

A series of numerical simulations was conducted to estimate the interaction among coastal protection infrastructure and multiscale sea level variability. We examined how a 50 cm sea level perturbation influences inundation around the perimeter of SF Bay while varying the duration of the perturbation from 2 days to a permanent change. We also examined the impact of shoreline infrastructure by comparing two seawall configurations, including the existing shoreline configuration and the coherent full-bay containment following the land boundary.

The tidal dynamics of SF Bay was successfully reproduced. We found that M_2 tide determines the MHHW pattern. Various spatial modes at different frequencies were captured by DMD, and each pattern can be interpreted using the corresponding physical processes. The study demonstrates the power of DMD to reveal the spatial structure of the tidal response to shoreline alteration by providing a holistic picture of the tidal dynamics that is unavailable with traditional methods. Although not exploited in this study due to the sinusoidal nature of the water levels, DMD has an additional advantage of predicting the growth/decay rate of each mode in the dynamic system. For longer data sets, or ones where unsteadiness is stronger, this capability will be particularly valuable.

While the multiday high water events had very small influence on the tidal dynamics (roughly 1–5% change, depending on the frequency), the reverse was not true. Based on fitting the numerical simulation results with a 1 d diffusive wave model, we found that tidal dynamics were of considerable importance in diffusing high water events and dissipating their peaks as they propagate into the Bay. Further, shoreline strategies, particularly the creation of accommodation space, increases the diffusive capabilities of the tides, leading to reductions in the peak water levels of multiday events.

Appendix A: Model Validation

We used the tidal boundary condition matching the phase and height of the stations of Monterey and Point Arena for the period of 1 January to 1 March 2010. The numerical simulation is validated by comparing the model results with the water level at nine stations recorded by NOAA (2016). The validation results are quantified in Table A1. The time series of four representative stations are shown in Figure A1. All of the comparisons are satisfactory. The tolerable errors may be caused by the inaccuracy in the bathymetry and the representation of the bottom roughness. The *r* denotes the Pearson correlation coefficient. Lags are

Table B2
Comparisons of the Water Level Between the Case of ExtLevHWL2 With 2 and 4 h Smoothing Periods to Show the Negligible Difference Between Them

Site number	*r*	RMS ratio
1	0.9997	0.9999
2°S	0.9998	1.0001
3°S	0.9998	1.0000
4°S	0.9998	0.9999
5°S	0.9998	0.9999
6°S	0.9998	0.9999
2°N	0.9997	0.9999
3°N	0.9997	0.9999
4°N	0.9998	0.9999
5°N	0.9998	1.0000
6°N	0.9998	1.0000
7°N	0.9998	1.0000
8°N	0.9997	1.0000

Table B3
Comparisons of the Water Level to Prove That There was Negligible Impact to Remove Minor Freshwater Discharge to the Bay

Site number	*r*	RMS ratio
1	0.9999	1.0043
2°S	1.0000	1.0038
3°S	1.0000	1.0039
4°S	0.9999	1.0041
5°S	0.9999	1.0042
6°S	0.9999	1.0043
2°N	0.9999	1.0043
3°N	0.9999	1.0044
4°N	0.9999	1.0044
5°N	0.9999	1.0046
6°N	0.9999	1.0049
7°N	0.9999	1.0054
8°N	0.9999	1.0064

computed as the time offset that maximizes the correlation coefficient. The RMS ratio is the ratio of model RMS amplitude to observed RMS amplitude.

Appendix B: Sensitivity of Model Inputs

A series of comparisons has been performed to check the sensitivity of the model to the smoothing period of HWL events, the interpolated ocean open boundary condition, and the minor river discharges. Table B1 shows that there was no significant difference between the water level between the tidal level interpolated from two tidal stations and the one generated by TPXO 7.2 (Egbert et al., 1994). The comparison was made to the eight sites distributed following the open boundary with equal distance. Table B2 shows that the water levels with 2 and 4 h smoothing periods were almost the same at 13 stations through the SF Bay. Table B3 shows that the water level was almost the same at the 13 stations through the bay if minor freshwater discharges were removed.

Acknowledgments
This work is supported by National Science Foundation grant (1541181). The first author would like to appreciate the inspiring discussion with Joel Tchoufag. Data are available through https://figshare.com/articles/Figures/5395138/1.

References

Berger, E., Sastuba, M., Vogt, D., Jung, B. & Amor, H. B. (2015). Estimation of perturbations in robotic behavior using dynamic mode decomposition. *Robotics*, *29*, 331–343.

Bertin, X., Li, K., Roland, A., Zhang, Y. J., Breilh, J. F., & Chaumillon, E. (2014). A modeling-based analysis of the flooding associated with xynthia, central bay of biscay. *Coastal Engineering*, *94*, 80–89.

Brunton, B. W., Johnson, L. A., Ojemann, J. G., & Kutz, J. N. (2016). Extracting spatial-temporal coherent patterns in large-scale neural recordings using dynamic mode decomposition. *Journal of Neuroscience Methods*, *258*, 1–15. https://doi.org/10.1016/j.jneumeth.2015.10.010

Buschman, F. A., Hoitink, A. J. F., Van Der Vegt, M., & Hoekstra, P. (2009). Subtidal water level variation controlled by river flow and tides. *Water Resources Research*, *45*, W10420. https://doi.org/10.1029/2009WR008167

Castanedo, S., Mendez, F. J., Medina, R., & Abascal, A. J. (2007). Long-term tidal level distribution using a wave-by-wave approach. *Advances in Water Resources*, *30*(11), 2271–2282. https://doi.org/10.1016/j.advwatres.2007.05.005

Chatterjee, A. (2004). An introduction to the proper orthogonal decomposition. *Current Science*, *78*(7), 808–817.

Chen, K. K., Tu, J. H., & Rowley, C. W. (2012). Variants of dynamic mode decomposition: Boundary condition, Koopman, and Fourier analyses. *Journal of Nonlinear Science*, *22*(6), 887–915.

Deltares (2016). *D-flow flexible mesh*. Retrieved from https://www.deltares.nl/en/software/delft3d-flexible-mesh-suite/

Doehring, C., Beagle, J., Lowe, J., Grossinger, R., Salomon, M., Kauhanen, P., . . . Bezalel, S. (2016). *San Francisco Bay shore inventory: Mapping for sea level rise planning* (SFEI Contrib. 779). Richmond, CA: San Francisco Estuary Institute.

Elias, E. P. L., & Hansen, J. E. (2013). Understanding processes controlling sediment transports at the mouth of a highly energetic inlet system (San Francisco Bay, CA). *Marine Geology*, *345*, 207–220. https://doi.org/10.1016/j.margeo.2012.07.003

Egbert, G., Bennett, A., & Foreman, M. (1994). Topex/poseidon tides estimated using a global inverse model: Topex/poseidon. *Journal of Geophysical Research*, *99*, 24821–24852.

Erikson, L. H., Wright, S. A., Elias, E., Hanes, D. M., Schoellhamer, D. H., & Largier, J. (2013). The use of modeling and suspended sediment concentration measurements for quantifying net suspended sediment transport through a large tidally dominated inlet. *Marine Geology*, *345*, 96–112. https://doi.org/10.1016/j.margeo.2013.06.001

Friedrichs, C., & Aubrey, D. (1988). Non-linear tidal distortion in shallow well-mixed estuaries: A synthesis. *Estuarine, Coastal and Shelf Science*, *27*, 521–545.

Friedrichs, C., & Aubrey, D. (1994). Tidal propagation in strongly convergent channels. *Journal of Geophysical Research*, *99*, 3321–3336.

Gallardo, D., Bevilacqua, R., & Sahni, O. (2014). Data-based hybrid reduced order modeling for vortex-induced nonlinear fluid–structure interaction at low Reynolds numbers. *Journal of Fluids and Structures*, *44*, 115–128. https://doi.org/10.1016/j.jfluidstructs.2013.10.012

Guo, L., Van Der Wegen, M., Jay, D. A., Matte, P., Wang, Z. B., Roelvink, D., & He, Q. (2015). River-tide dynamics: Exploration of nonstationary and nonlinear tidal behavior in the Yangtze River estuary. *Journal of Geophysical Research: Oceans*, *120*, 3499–3521. https://doi.org/10.1002/2014JC010491

Henderson, F. M. (1996). *Open channel flow*. New York, NY: Macmillan.

Holleman, R. C., & Stacey, M. T. (2014). Coupling of sea level rise, tidal amplification, and inundation. *Journal of Physical Oceanography*, *44*(5), 1439–1455. https://doi.org/10.1175/JPO-D-13-0214.1

Horsburgh, K., & Wilson, C. (2007). Tide-surge interaction and its role in the distribution of surge residuals in the north sea. *Journal of Geophysical Research*, *112*, C08003. https://doi.org/10.1029/2006JC004033

Idier, D., Paris, F., Le Cozannet, G., Boulahya, F., & Dumas, F. (2017). Sea-level rise impacts on the tides of the European shelf. *Continental Shelf Research*, *137*, 56–71.

Jay, D., Leffler, K., Diefenderfer, H., & Borde, A. (2015). Tidal-fluvial and estuarine processes in the lower Columbia River: I. Along-channel water level variations, Pacific Ocean to Bonneville Dam. *Estuaries and Coasts*, *38*(2), 415–433.

Jovanović, M. R., Schmid, P. J., & Nichols, J. W. (2014). Sparsity-promoting dynamic mode decomposition. *Physics of Fluids*, *26*(2), 024103.

Le Provost, C. (1991). Generation of overtides and compound tides (review). In B. Parker (Ed.), *Tidal hydrodynamics* (pp. 269–295). New York, NY: John Wiley.

Lin, N., Emanuel, K., Oppenheimer, M., & Vanmarcke, E. (2012). Physically based assessment of hurricane surge threat under climate change. *Nature Climate Change*, *2*(6), 462–467.

Martyr-Koller, R. C., Kernkampb, H., van Dam, A., van der Wegen, M., Lucasc, L., Knowlesc, N., . . . Fregoso, T. (2017). Application of an unstructured 3D finite volume numerical model for hydrodynamic and water-quality transport in the San Francisco Bay-Delta. *Estuarine, Coastal and Shelf Science*, *192*(6), 86–107.

Nidzieko, N. J. (2010). Tidal asymmetry in estuaries with mixed semidiurnal/diurnal tides. *Journal of Geophysical Research*, *115*, C08006. https://doi.org/10.1029/2009JC005864

NOAA (2016). *NOAA tides and currents*. Retrieved from https://tidesandcurrents.noaa.gov/

Parker, B. B. (1991). *Tidal hydrodynamics*. New York, NY: John Wiley.

Parker, B. B. (1984). *Friction effects on the tidal dynamics of a shallow estuary* (PhD thesis, 292 pp.), Baltimore, MD: John Hopkins University.

Pelling, H. E., & Green, J. M. (2014). Impact of flood defences and sea-level rise on the European shelf tidal regime. *Continental Shelf Research*, *85*, 96–105.

Pickering, M., Horsburgh, Blundell, K. J., Hirschi, J.-M., Nicholls, R., Verlaan, M., & Wells, N. (2017). The impact of future sea-level rise on the global tides. *Continental Shelf Research*, *142*, 50–68.

Pickering, M., Wells, N., Horsburgh, K., & Green, J. (2012). The impact of future sea-level rise on the European shelf tides. *Continental Shelf Research*, *35*, 1–15.

Proctor, J., & Eckhoff, P. (2015). Discovering dynamic patterns from infectious disease data using dynamic mode decomposition. *International Health*, *7*(2), 139–145.

Proudman, J. (1953). *Dynamical oceanography*. London, UK: Methuen.

Pugh, D. (2004). *Changing sea levels: Effects of tides, weather and climate*. Cambridge, UK: Cambridge University Press.

Pugh, D. T. (1987). *Tides, surges and mean sea-level: A handbook for engineers and scientists* (Vol. 8, 1273 pp.). Chichester, UK: John Wiley. http://doi.org/10.1016/0278-4343(88)90006-4

Sassi, M. G., & Hoitink, A. J. F. (2013). River flow controls on tides and tide-mean water level profiles in a tidal freshwater river. *Journal of Geophysical Research: Oceans*, *118*, 4139–4151. http://doi.org/10.1002/jgrc.20297

Schmid, P. J. (2010). Dynamic mode decomposition of numerical and experimental data. *Journal of Fluid Mechanics*, *656*(4), 5–28. http://doi.org/10.1017/S0022112010001217

Song, D., Wang, X. H., Kiss, A. E., & Bao, X. (2011). The contribution to tidal asymmetry by different combinations of tidal constituents. *Journal of Geophysical Research*, *116*, C12007. http://doi.org/10.1029/2011JC007270

USGS (2016). *USGS current water data for the nation*. Retrieved from https://waterdata.usgs.gov/nwis/rt

Walters, R. A., & Werner, F. E. (1991). Nonlinear generation of overtides, compound tides, and residuals. In B. B. Parker (Ed.), *Tidal hydrodynamics* (pp. 297–320). New York, NY: John Wiley.

Wang, Z. B., Jeuken, C., & Vriend, H. J. D. (1999). *Tidal asymmetry and residual sediment transport in estuaries: A literature study and application to the Western Scheldt* (Hydraulic Rep. Z2749). Delft, the Netherlands: WL Delft Hydraulics.

Woodworth, P. L., Blackman, D. L., Pugh, D. T., & Vassie, J. M. (2005). On the role of diurnal tides in contributing to asymmetries in tidal probability distribution functions in areas of predominantly semi-diurnal tide. *Estuarine, Coastal and Shelf Science*, *64*(2–3), 235–240. https://doi.org/10.1016/j.ecss.2005.02.014